JOURNAL OF SPACECRAFT AND ROCKETS
Vol. 32, No. 3, May–June 1995

Analysis of Flowfields over Missile Configurations at Subsonic Speeds

J. A. Ekaterinaris*
Naval Postgraduate School, Monterey, California 93943

Flowfields over missile configurations at subsonic speeds and high angle of attack are computed with a Navier–Stokes flow solver using overset grids. The accuracy of the computed solutions is first validated for flows at high incidence over a fuselage-wing and a fuselage-canard-wing configuration. The effects of grid density and turbulent versus laminar solutions are assessed by comparison with detailed experimental surface pressures. Development of vortex breakdown over the wing is predicted in accordance with the experiment. Delay of vortex breakdown over the wing caused by the presence of the canard was also captured by the numerical solution. The computed surface pressures are in good agreement with the experiment. Solutions for a complete missile configuration with fins and tails at 45-deg roll are also obtained for subsonic flow at high incidence. The computed normal force and pitching moment are in good agreement with available measurements. The effect of the fin deflection on the development of the vortical flowfield is investigated. It is found that the flowfield in the fin and gap regions can be of primary importance to the overall development of the forebody flowfield.

Nomenclature

a_∞	= freestream speed of sound
b_c	= canard root span
b_w	= wing root span
C	= wing chord
C_M	= pitching-moment coefficient
C_N	= normal-force coefficient
C_p	= $2(p - p_\infty)/\rho_\infty M_\infty^2$, pressure coefficient
D	= fuselage diameter
M_∞	= U_∞/α_∞, freestream Mach number
p	= pressure
R	= fuselage radius
Re_C	= $U_\infty C/\nu_\infty$, Reynolds number based on the wing chord length
Re_D	= $U_\infty D/\nu_\infty$, Reynolds number based on the fuselage diameter
U_∞	= freestream speed
x, y, z	= Cartesian coordinates
α	= angle of attack
δ	= fin deflection angle
ρ	= density
ϕ	= angular location in the circumferential direction

Introduction

MODERN missile configuration designs have the tendency to reduce the area of control surfaces, such as fins and tails, in order to achieve better aerodynamic performance characteristics in flight. As a result of these design requirements, stability problems could appear at high-angle-of-attack launch conditions, where the speed is in the low subsonic regime. Another situation where stability and controllability could be important is missile deployment from aircraft maneuvering at high angle of attack. For this case, wing-store interference and low controllability may cause serious safety problems. Therefore, investigations of the flowfield over missile configurations at high incidence and subsonic flow and understanding of the effect that control surfaces have on the stability characteristics and the development of flow asymmetries are crucial to efforts in improving the design of future-generation missiles.

Received April 11, 1994; presented as Paper 94-1915 at the AIAA 12th Applied Aerodynamics Conference, Colorado Springs, CO, June 20–23, 1994; revision received Aug. 4, 1994; accepted for publication Aug. 10, 1994.

*Research Associate Professor, Department of Aeronautics and Astronautics. Member AIAA.

Until now most of the missile design process has been based on information obtained from wind-tunnel and flight test data, usually in the form of integrated loads. Engineering methods, which provide predictions of the missile forces and moments for low angles of attack, are used to supplement new design concepts for the low-angle-of-attack regime. At high angles of incidence, the flowfield is dominated by strong vortices. Large side forces and loss of control effectiveness may result from asymmetric vortices. Better understanding of the flowfield under these conditions can be obtained with detailed experimental studies, including flow visualization and application of computational fluid dynamics (CFD) methods. It is important for the success of numerical methods that all the essential geometrical details be modeled, and that the viscous-dominated flow regions be resolved adequately.

Grid generation is a difficult task for the application of CFD methods to complex configurations. For structured grid methods, the multiblock and overset grid techniques may be used. As far as grid generation is concerned, the multiblock grid strategy is more time-consuming and requires special attention to the boundary-condition specification. Therefore, in the present investigation an overset approach[1] is used. The overset method provides flexibility in decomposing the computational domain, and facilitates the grid generation over complex geometries. This method has been applied with success for the simulation of complex flow problems, such as flows over complete aircraft configurations.[2]

The missile configuration of interest consists of the missile body with fins and tails. The total length of the missile body is 22.6 body diameters. The fins are 67-deg sweep delta planforms with root chord length 2.5 diameters. The tails are 45-deg sweep trapezoidal planforms with root chord length 3 diameters and span 1.1 body diameters. The tails are fixed on the missile body, but the fins are free to rotate, and they are usually set at an angle of incidence for low-speed, high-angle-of-attack launch. For this missile configuration there exist only a limited number of experimental data for forces and moments.[3] Further experimental investigations by Naval Air Warfare Center (NAWC), China Lake, to obtain surface oil flow data are underway. Experimental measurements for missile configurations have been obtained mainly for supersonic speeds.

In order to demonstrate the applicability of the solution method and to assess the grid resolution requirements, the flow over a canard-wing-fuselage configuration is computed first. The definition of the geometry and surface pressure measurements for this configuration are given in Ref. 4. This flowfield includes many of the features of the flowfield over a missile, such as vortex interaction and development of vortex breakdown. The flow over a similar close-coupled canard-wing configuration at transonic speeds $M_\infty = 0.9$ and low

angles of incidence $\alpha = 0$ deg to $\alpha = 12$ deg has been investigated experimentally[5,6] and numerically.[7] The numerical solution[7] was in good agreement with the experimental measurements,[5,6] and delay of vortex breakdown due to the presence of the canard was obtained. In addition, other experimental studies by Lancey and Chorney,[8] Dollyhigh,[9] Er-El and Seginer,[10] and Calarese[11] investigated the canard-wing vortex system and the mechanisms of the canard-wing interaction. Experimental[12] and numerical[13] investigations for flows over missile configurations at supersonic speeds have been also performed.

Numerical Implementation

The OVERFLOW[14] code is used for the numerical solutions. In this code the overset chimera technique is implemented. Among the various options available in the code, the two-factor scheme is chosen. This scheme uses Steger–Warming[15] flux-vector splitting for discretization in the streamwise direction and central differences for the other two directions. Implicit and explicit smoothing are used for the central-differencing directions. For turbulent flow solutions, the Baldwin–Lomax[16] eddy-viscosity model with the modifications suggested by Degani and Schiff[17] is used for the computation of vortical flows. The solution initiates with freestream flow everywhere and marches in time. On the solid surface the nonslip boundary condition is imposed for the velocities, and the density and pressure are obtained by simple extrapolation from the interior. At the inflow and outflow, boundary data are obtained by one-dimensional Riemann invariant extrapolation.

Detailed descriptions of the geometry of the missile and the fuselage-canard-wing configuration are given in Refs. 3 and 4, respectively. For both configurations, the complex surface geometry is subdivided into simpler components, for which surface and flowfield grid generation may be achieved faster and in a more straightforward manner than for the complete configuration. The numerical mesh for the components such as fins, tails, and the missile fuselage are generated first. Various components, such as wings or tails, which are physically attached to the fuselage, are inserted in the global fuselage grid. The region of the global grid where a component is inserted is blanked out from the solution. The blanked-out region is referred to as a hole region. The inserted grid communicates with the outer grid by means of boundary data transfer at the outer-grid boundary. Similarly, the outer grid receives boundary values at the hole boundaries from the inserted grid. Typically, at least one-cell overlap is necessary for information exchange or updating the solution. The grids, however, are not required to be aligned at the interfaces. At the boundaries where information transfer occurs, the flow variables are obtained from the neighboring grid by interpolation. The Pegasus code,[1] which is used to preprocess the grid data, provides the interpolation stencils at the grid interfaces and defines regions where holes are cut by one grid in another.

The entire mesh over the fuselage-canard-wing configuration is constructed by attaching the canard and wing grids to the fuselage grid. Similarly, separate grids are used for the fins and the tails of the missile. The gap region between the fin and the fuselage is also modeled, using a separate grid block. The grid generation procedure is briefly described below.

Grid Generation

The grid over the canard-wing-fuselage configuration of Ref. 4 is partitioned into blocks (see Fig. 1). Partitioning of the grid into blocks helps to reduce the in-core memory requirements and allows local grid refinement in selected flow regions. The three blocks over the fuselage are not point-matched as multiblock grids, but they have the grid lines distributed differently for each block so that better resolution of local flow features can be achieved. The first block consists of a $51 \times 71 \times 71$-point grid along the streamwise, circumferential, and normal directions, respectively. This block includes the fuselage apex and the canard region. The second block, which includes the wing region, consists of a $42 \times 81 \times 75$-point grid. In these two blocks holes are cut by the canard and wing grids. The third block consists of a $28 \times 73 \times 71$-point grid, which includes the downstream part of the fuselage and provides sufficient resolution

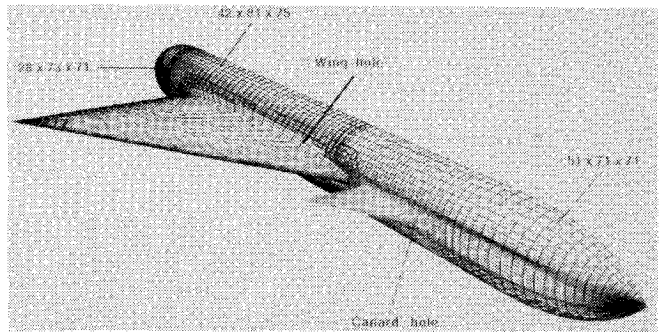

Fig. 1 Grid partition for the canard-wing-wing configuration.

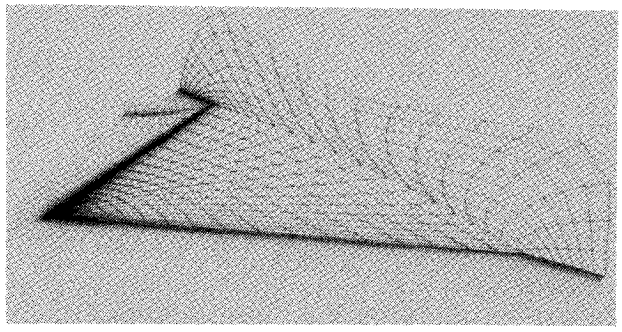

Fig. 2 Surface and field C-O-type grid around the canard.

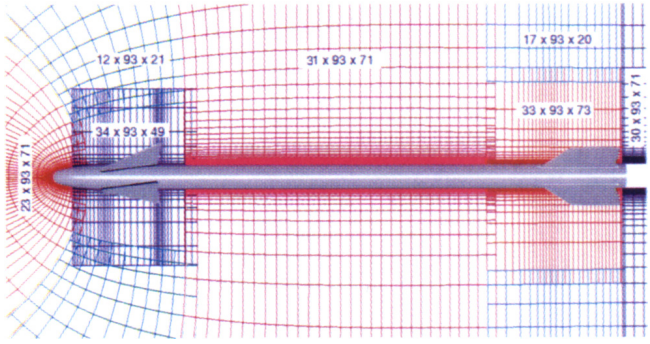

Fig. 3 Grid partition for the complete missile configuration.

for the wake of the wing. For all grids, the distance of the first point from the body surface is 0.00001 fuselage diameters.

The canard and wing grids (Fig. 2) are of C-O type. They are periodic grids, which wrap around the planform. These grids have a singular line at the trailing-edge apex. The canard grid is a $32 \times 50 \times 47$-point grid along the spanwise, the chordwise periodic, and the normal direction, respectively. Similarly, the wing grid has $39 \times 87 \times 45$-points. Both grids provide approximately the same resolution per unit area of the planform and extend almost one chord length beyond the surface. The canard and wing surfaces include part of the fuselage wing junction, as shown in Figs. 1 and 2. The grid topology chosen for the wing and the canard enables one to resolve the canard-wing and fuselage-wing junction flow and provides sufficient grid density for good capturing of the wake flow. In the normal direction, the first point is located 0.00001 fuselage diameters away from the surface. For both the body and canard-wing grids, the near-wall flow region is resolved with 25 to 30 points. The Pegasus code[1] is used to cut holes in the fuselage grid at the locations where the canard and wing are inserted. The hole boundaries cut in the fuselage grid by the canard and the wing (see Fig. 1) are outside the near-wall viscous-flow regions. The wing and canard leeward-side vortical-flow region is resolved by the outer fuselage grid. This grid arrangement is found to be optimal because it provides good communication for the viscous layers and enables efficient interfacing away from regions of large flow gradients.

The grid over the missile body is also partitioned into several blocks. The grid partitioning for the complete missile configuration is shown in Fig. 3. In the near-wall region, the same grid quality

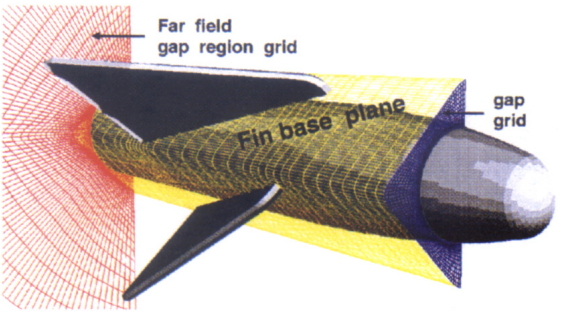

Fig. 4 Detail of the fin gap region.

characteristics given for the canard-wing configuration grids are used. Different grid densities are used in the circumferential and normal directions for the various blocks over the missile fuselage, as indicated in Fig. 3, and, as before, there is no grid-point matching at the interfaces. The tail grids are attached to the missile body as described before, and the grids over the tails are C-O-type spherical, periodic grids. Special attention is given to accurate modeling of the geometry in the region of the deflected fins. The fin apex extends forward of the region where the ogive part of the nose merges with the straight missile body. As a result, even with zero fin deflection angle there exists a gap between the missile body and the fin base. When the fins are deflected, a larger gap under the fin is created. In this region the forebody flow is significantly disrupted. Therefore, it is necessary to model accurately the geometry between the fin and the missile fuselage and to provide sufficient grid resolution.

For the fin gap region, a separate cylindrical grid block, shown in Fig. 4, is generated. The inner grid surface defines the missile body surface, and the grid lines at the location of the fin base form oblique flat surfaces. The fin grid consists of two parts, a C-O-type periodic grid for the windward and leeward sides, and a viscous mesh at the fin base, which coincides with the flat surface generated in the gap-region grid. The fin-base viscous grid receives boundary information from the gap-region grid. The concentration of grid lines at the fin base region enables efficient communication between the two grids. It was found that high grid resolution is required for the gap grid at the fin-base interface region in order to establish good communication. Part of the gap-region grid is also used to resolve the vortical flow generated in the gap region at high incidence. The present construction of the gap-region grid makes it possible to connect the fins at any deflection angle by interfacing fin grids with the gap-region grid. For large deflection angles, part of the fin field grid extends beyond the symmetry plane. This part of the fin field grid is blanked out by the fuselage grid in a longitudinal plane inboard of the symmetry plane.

The tails are attached to the fuselage as described before. A $69 \times 65 \times 46$ point C-O-type spherical, periodic grid is used for each tail. The flow around the fuselage-tail junction is resolved by the tail grid. At the end of the fuselage a cylindrical sting that extends to the outflow of the computational domain is used. The outer boundaries of the missile fuselage grid are located at approximately five missile body lengths.

Results

Canard-Wing-Fuselage Configuration

In Ref. 4, the freestream speed is $(M_\infty)_{\text{exp}} \approx 0.11$. The flow over the canard-wing-fuselage configuration is computed at a Mach number $M_\infty = 0.2$, which is higher than the experimental value, in order to achieve better convergence rates. In Refs. 18 and 19 solutions over delta wings have been obtained at a higher freestream speed than in the experiment, and the computed surface distributions were in good agreement with the experiment. The Reynolds number based on the wing root chord is the same as the experiment, $Re_c = 1.4 \times 10^6$. The Reynolds number based on the fuselage diameter is $Re_D = 0.23 \times 10^6$, and the forebody flow is expected to be mostly laminar. The effect of turbulence modeling is investigated, and both laminar and turbulent solutions are computed. Flowfields without canard and with canard are also computed. All the solutions are computed as half-body solutions, and symmetry conditions are applied.

Flow at $\alpha = 19.3$ deg

The computed flowfield for the experimental case at an angle of attack of $\alpha = 19.3$ deg and $Re_c = 1.4 \times 10^6$ over the wing-fuselage configuration is presented first. The computed leeward-side vortical flowfields obtained from the laminar and the turbulent solution are shown in Fig. 5. In this figure, the locations of the fuselage and wing vortices are shown, and the surface streamlines indicate the separation and reattachment lines. The fully turbulent solution predicts a breakdown location downstream of the experimentally determined position. However, the breakdown location obtained from the laminar solution is in closer agreement with the experiment. The flow in the experiment was not tripped, and transitional effects may be of importance at the wing trailing edge. Comparison of the computed surface pressure coefficients (not shown here) shows that the laminar solution is in better agreement with the experiment. Therefore, all the other solutions for this configuration are computed as laminar.

A solution with increased grid resolution for the leeward side part of the fuselage grid in the wing region is also computed. For both baseline and refined-grid solutions, the near-wall viscous flow over the wing is resolved by the same wing grid. As the wing vortex lifts off the wing surface, the outer fuselage grid is used to resolve the wing leeward-side vortical flowfield. Therefore, only the fuselage grid in the wing region is locally refined. For the windward side, a $42 \times 29 \times 75$-point grid with the same resolution as the baseline grid is used. For the leeward side, the grid is refined in the vortical flow region identified by the baseline grid solution. Grid refinement is performed in both circumferential and normal directions, and a $42 \times 75 \times 91$-point grid is obtained. The leeward-side vortical flowfields computed by the baseline and the refined-grid solutions are compared in Fig. 6. Both solutions predict breakdown at approximately the same location, and the refined grid shows a slightly larger breakdown region. It is found that the prediction of the surface pressure coefficients improves with the refined grid, and that grid is used.

The computed and measured surface pressure coefficients for several streamwise locations along the fuselage are compared in Fig. 7. The streamwise locations where the computations are compared with the experiment are given as distances from the wing trailing edge normalized by the wing chord. At the fuselage-wing

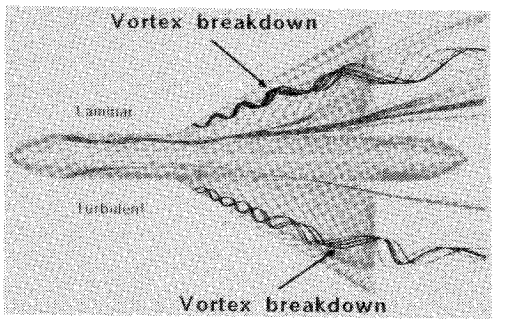

Fig. 5 Leeward-side computed flowfield over the fuselage-wing configuration; $(M_{\text{exp}})_\infty = 0.11, M_\infty = 0.2, \alpha = 19.3$ deg, $Re_D = 1.4 \times 10^6$.

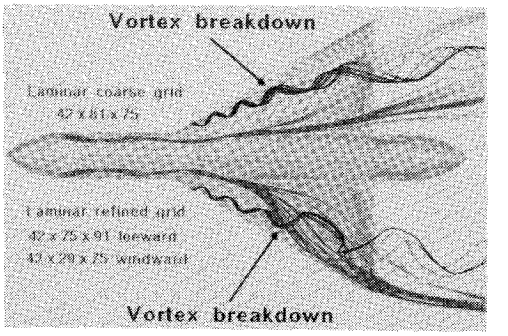

Fig. 6 Effect of grid refinement on the leeward-side flowfield over the fuselage-wing configuration; $(M_{\text{exp}})_\infty = 0.11, M_\infty = 0.2, \alpha = 19.3$ deg, $Re_D = 1.4 \times 10^6$.

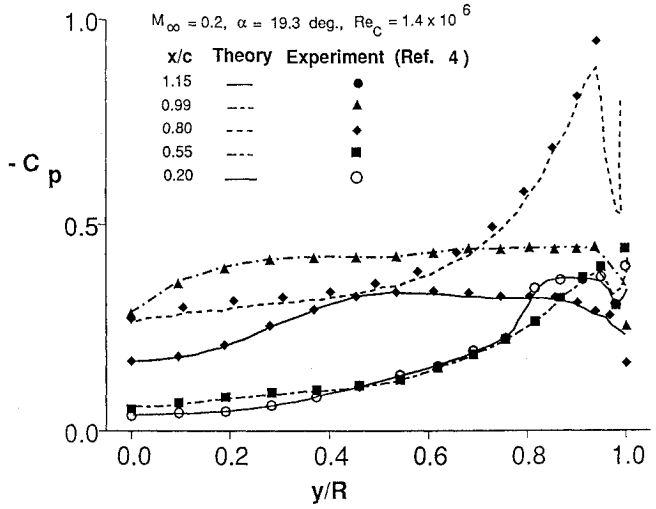

Fig. 7 Comparison of the fuselage computed and measured surface pressure coefficient.

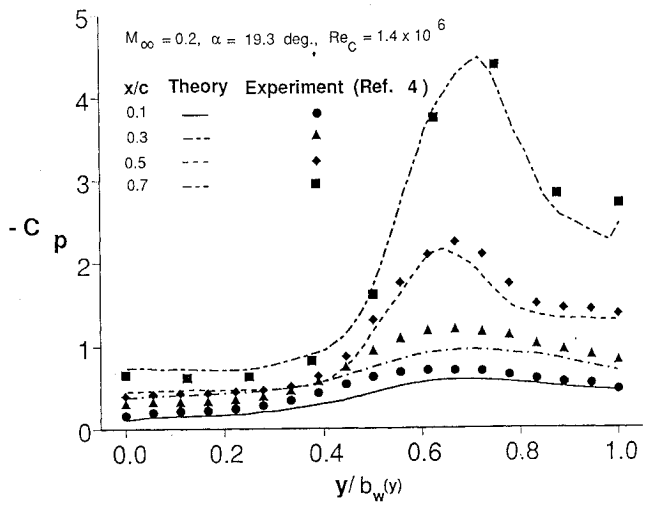

Fig. 8 Comparison of the wing computed and measured surface pressure coefficient.

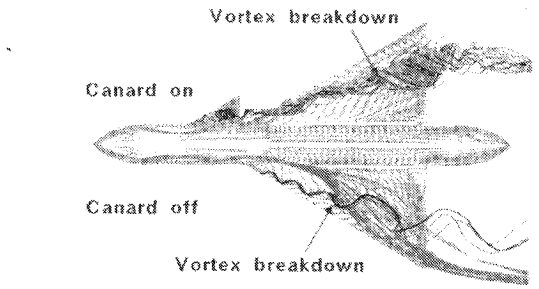

Fig. 9 Effect of the canard on the leeward-side flowfield; $(M_{exp})_\infty$ = 0.11, M_∞ = 0.2, α = 19.3 deg, $Re_D = 1.4 \times 10^6$.

junction, the surface flow is computed by the wing grid. The rest of the surface flow is computed by the fuselage grid. The comparisons of Fig. 7 demonstrate that the surface pressures are predicted fairly accurately. The computed surface pressure coefficient for the wing section is compared with the experimental measurements in Fig. 8. Good agreement is obtained for the part of the flowfield without vortex breakdown, but the computed suction peaks are lower than the experimentally measured suction peaks for the locations where vortex breakdown has occurred.

The flowfield for the fuselage-canard-wing configuration at α = 19.3 deg is computed next. The effect of the canard on the development of the leeward-side flowfield is shown in Fig. 9. In the same figure the leeward-side flowfield computed with the canard

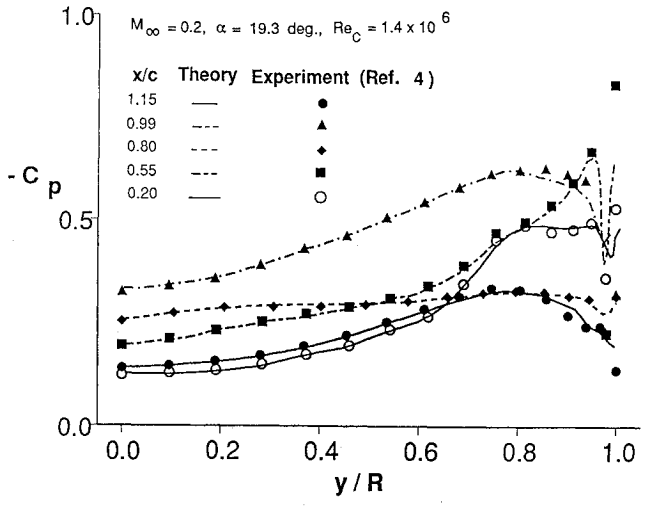

Fig. 10 Comparison of the fuselage computed and measured surface pressure coefficient.

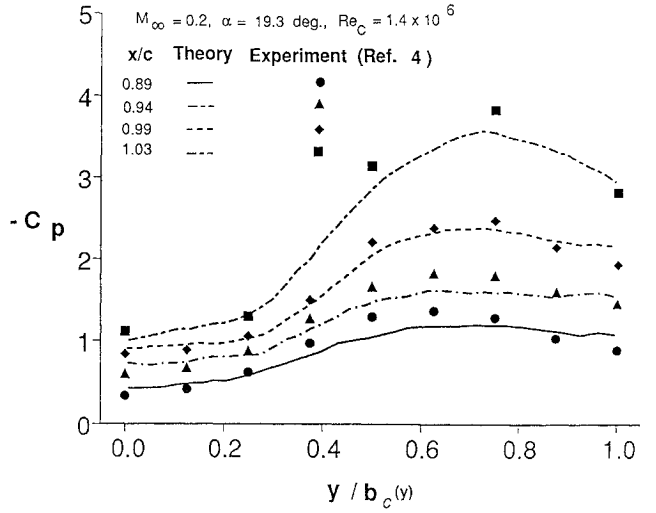

Fig. 11 Comparison of the canard computed and measured surface pressure coefficient.

off is also shown. The canard creates a suction upstream of the wing. Because of the decreased pressure gradient, the wing vortex breakdown location is delayed to a location downstream of where it was without the canard. The vortical flowfields of the forebody and the canard merge into the wing leading-edge vortical flowfield. The computed surface pressure coefficients for the fuselage, the canard, and the wing are compared with the experimental data in Figs. 10–12, respectively. Figure 10 shows that good agreement with the experiment is obtained for most streamwise locations along the fuselage. The computed surface pressure coefficients over the canard (Fig. 11) are lower than the measurements, but good qualitative agreement is obtained. The comparisons of the surface pressure coefficients of Fig. 12 indicate that a more diffused vortex is obtained in the computed solution and the agreement with the measurements is only qualitative. It appears that the relatively weak canard vortex is diffused.

Flow at α = 29.1 deg

A solution at α = 29.1 deg is presented next. At this angle of attack the computed solution for the fuselage-wing configuration predicts vortex breakdown very close to the wing apex. The computed flow with the canard, as shown in Fig. 13, demonstrates that vortex breakdown onset is delayed and occurs at approximately one-quarter chord from the apex. The leeward-side flow structure at α = 29.1 deg is similar to the one obtained at α = 19.3 deg. The computed surface pressure coefficient over the wing is compared with the measurements in Fig. 14. Qualitative agreement with the

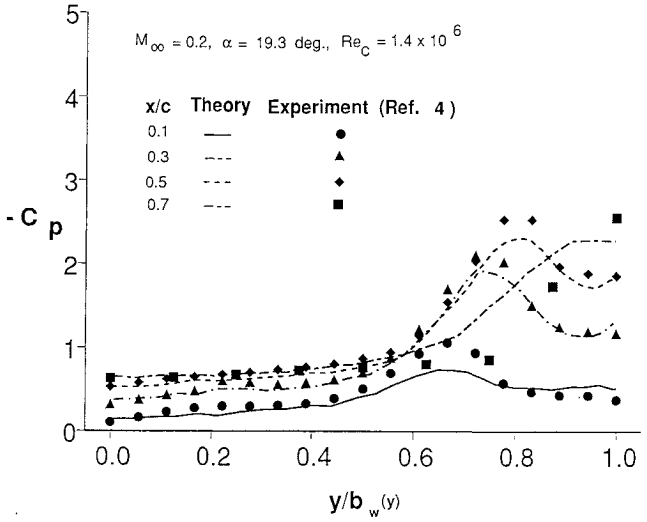

Fig. 12 Comparison of the wing computed and measured surface pressure coefficient.

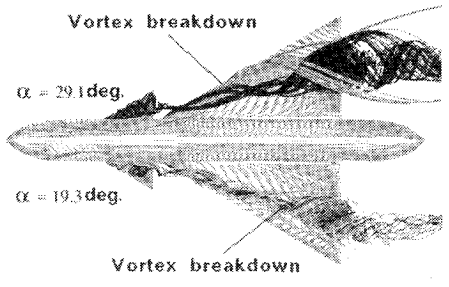

Fig. 13 Effect of angle of attack on the leeward-side flowfield; $(M_{exp})_\infty = 0.11, M_\infty = 0.2, \alpha = 19.3$ and 24.1 deg, $Re_D = 1.4 \times 10^6$.

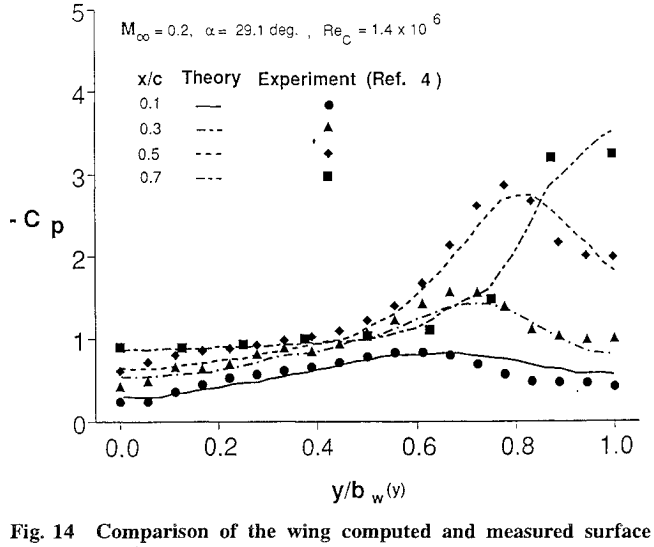

Fig. 14 Comparison of the wing computed and measured surface pressure coefficient.

measurements is obtained at this higher angle of incidence, but the computed surface pressure coefficient underpredicts the experimental data in the vortex breakdown region.

Missile Configuration

The missile flowfield is computed for 45-deg roll. This configuration is referred to as the × configuration. For it, symmetry can be applied, and only half-body, symmetric solutions are required. In contrast, computation of the 0-deg roll (+ configuration) with deflected fins requires a full-body solution. Flowfield solutions with fins on and with fins off have been computed. The computed flowfields without fins are dominated by the forebody

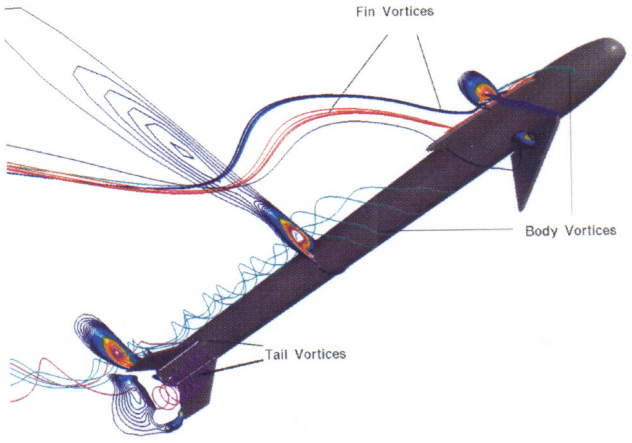

Fig. 15 Computed flowfield and helicity density over the missile; $M_\infty = 0.3, \alpha = 45.0$ deg, $Re_D = 0.95 \times 10^6, \delta = 10$ deg.

vortices, and only the aft portion is affected by the tail vortical flowfield. The flowfield over the complete missile configuration was computed for two fin deflection angles: $\delta = 10$ deg, and $\delta = 20$ deg. All computations were performed at $M_\infty = 0.3$, $\alpha = 45$ deg, and $Re_D = 0.95 \times 10^6$, which are typical conditions for missile launch. The Reynolds number based on the diameter is high enough to assume fully turbulent flow. The Baldwin-Lomax model with the modifications suggested by Degani and Schiff for the computation of vortical separated flows is used to compute the eddy viscosity.

The vortex system over the complete missile configuration for a fin deflection angle $\delta = 10$ deg is shown in Fig. 15. In this figure the helicity density at several cross-flow planes is shown. The helicity density in the fin region shows development of a vortical region over the upper fin. Due to the high angle of incidence, the flowfield over the fins is highly separated and there is no coherent leading-edge vortex. The forebody vortex and the vortices generated in the gap between the fins and the fuselage merge into a single vortical region over the upper fin. The fin and forebody vortices lift away from the missile surface and spiral along the freestream. Downstream of the fins, another vortex is generated by the missile body, which merges with the tail vortical flowfield. In the region between the two tails a recirculatory flow region is developed, while over the upper tail a coherent leading-edge vortex is obtained.

The flow in the gap between the fins and the missile fuselage is quite complex. A cross-flow view for two different deflection angles is shown in Figs. 16a and 16b. In these figures the location of the holes where the fins are inserted is indicated. On the left side the helicity density is shown. The dashed lines mark the regions of negative helicity. The large region of negative helicity for $\delta = 20$ deg is caused by reverse flow. Variations of the fin deflection angle cause large changes in this part of the flowfield.

Figure 16 shows that significant changes of the flowfield structure in the fin region occur when the fin deflection angle increases. Analogous changes of the computed surface flow pattern in this region are observed in Figs. 17 and 18. The computed surface flow pattern of the missile fuselage for a fin deflection angle $\delta = 10$ deg is shown in Figs. 17a and 17b. Figure 17a shows the surface flow on the leeward or upper surface of the fuselage for circumferential locations from $\phi = 0$ deg to $\phi = 90$ deg. One separation line corresponding to the primary forebody vortex is observed upstream from the fin in the nose region. A second separation line and a reattachment line exist in the region between the upper fin and the symmetry plane $\phi = 0$ deg. This separation and reattachment is caused by a vortex that is generated at the gap between the upper fin and the missile fuselage as shown in Fig. 16a. Similarly, for the windward side the computed surface flow of Fig. 16b for $\phi = 90$ deg to $\phi = 180$ deg also shows separation and reattachment lines between the lower fin and the $\phi = 90$ deg line.

At the higher fin deflection angle $\delta = 20$ deg, the upper and lower surface patterns shown in Figs. 18a and 18b, respectively, indicate that significant changes of the surface flow pattern are caused by the increase of the fin deflection angle. Upstream from the upper fin two

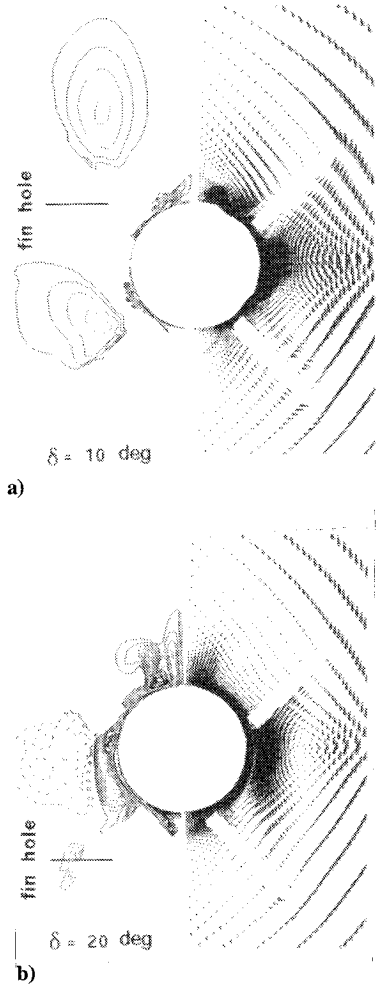

Fig. 16 Cross-flowfield detail in the fin-fuselage gap region; $M_\infty = 0.3$, $\alpha = 45.0$ deg, $Re_D = 0.95 \times 10^6$: a) $\delta = 10$ deg and b) $\delta = 20$ deg.

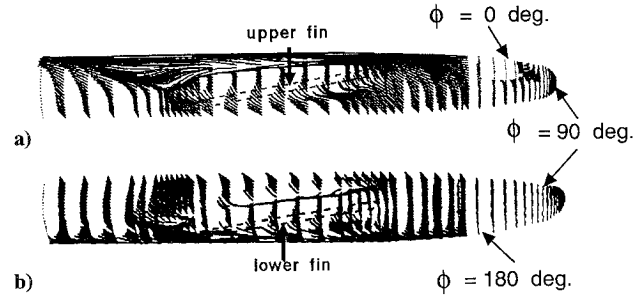

Fig. 17 Surface flow pattern over the missile forebody with $\delta = 10$ deg: a) leeward-side (upper) surface and b) windward-side (lower) surface.

separation lines are observed. Inspection of the computed velocity field and helicity density in crossflow planes upstream of the fin shows that under the forebody vortex a secondary separation and a secondary vortex have been formed. Highly separated flow over the upper fin produces a complex vortical flowfield over the upper fin and in the region between the two fins. However, the surface flow between the upper fin and the symmetry plane remains mostly attached. Only one separation line caused by the primary forebody vortex is formed close to the symmetry plane. A complex separation and reattachment pattern is obtained in the region downstream of the upper fin. On the lower surface, upstream from the lower fin, flow separation and attachment lines are obtained as a result of a wing-body junctionlike recirculatory flow development. Downstream from the lower fin an attachment line is obtained from flow that was separated over the lower fin and reattaches downstream on the missile fuselage.

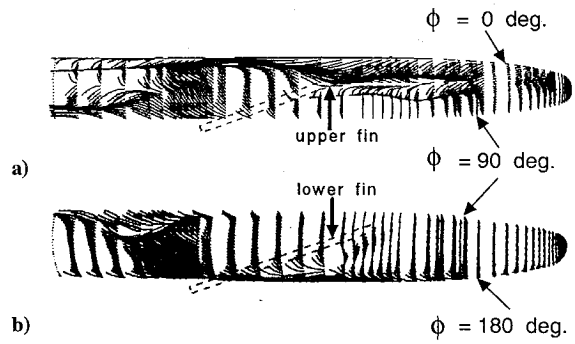

Fig. 18 Surface flow pattern over the missile forebody with $\delta = 20$ deg: a) leeward-side (upper) surface and b) windward-side (lower) surface.

In the absence of other available experimental data, the integrated loads are compared with these experiments. The computed normal force at $\delta = 20$ deg is $C_N = 34.1$, and the pitching moment is $C_M = -76.5$. These values are close to the experimental values of $C_N = 32$ and $C_M = -80$ reported in Ref. 3. For the case $\delta = 10$ deg, $C_N = 32.7$ and the pitching moment is $C_M = -71.9$.

Concluding Remarks

An overset grid method was used with a Navier–Stokes solver for the numerical calculation of flowfields over missile configurations at high incidences. Solutions for a fuselage-wing and a fuselage-canard-wing configuration showed reasonably good agreement with experimental measurements. The computed flowfields demonstrate that a close-coupled canard-wing system has the effect of delaying vortex breakdown over the wing. The computed flowfield over the missile indicates that the complex flow pattern generated in the gap region between the fuselage and the deflected fins plays an important role in the development of the flowfield over a missile at high incidence. Appropriate geometry modifications can produce improved flow characteristics of the forebody flow. As a result, enhanced stability and controllability at high incidences may be obtained. Solutions for 0-deg roll angle and full-body solution are still required in order to investigate vortex asymmetries and development of self-induced unsteady flow.

Acknowledgment

This investigation was supported by the Naval Air Warfare Center, Weapons Division, China Lake, California.

References

[1]Benek, J. A., Buning, P. G., and Steger, J. L., "A 3D Chimera Grid Embedding Technique," AIAA Paper 85-1523, July 1985.

[2]Cummings, R. M., Rizk, Y. M., Schiff, L. B., and Chaderjian, N. M., "Navier–Stokes Predictions of the Flowfield around the F-18 (HARV) Wing and Fuselage at Large Incidence," AIAA Paper 90-0099, Jan. 1990.

[3]Smith, E. H., Hebbar, S. K., and Platzer, F. M., "Aerodynamic Characteristics of a Canard-Controlled Missile at High Angles of Attack," AIAA Paper 93-0763, Jan. 1993.

[4]Bergmann, A., Hummel, D., and Oenkel, H.-C., "Vortex Formation over a Close-Coupled Canard-Wing-Body Configuration in Unsymmetric Flow," *Fluid Dynamics Panel Symposium on Vortex Flow Aerodynamics*, 1990, pp. 14-1–14-14 (AGARD Paper 14).

[5]Gloss, B. B., and Washburn, K. E., "Load Distribution on a Close-Coupled Wing Canard at Transonic Speeds," *Journal of Aircraft*, Vol. 15, No. 4, 1978, pp. 234–239.

[6]Gloss, B. B., and Washburn, K. E., "A Study of Canard-Wing Interference Using Experimental Pressure Data at Transonic Speeds," NASA TP 1355, Jan. 1979.

[7]Tu, E. L., "Navier–Stokes Simulations of a Close-Coupled Canard-Wing-Body Configuration," *Journal of Aircraft*, Vol. 29, No. 5, 1992, pp. 830–838.

[8]Lacey, D. W., and Chorney, S. J., "Subsonic Aerodynamic Characteristics of Close-Coupled Canards with Varying Area and Position Relative to a 50 deg Sweep Wing," TN-AL-199, Naval Ship Research and Development Center, 1971.

[9]Dollyhigh, S. M., "Static Longitudinal Aerodynamic Characteristics of Close-Coupled Wing-Canard Configurations at Mach Numbers from 1.60 to 2.86," NASA TN D-6597, Dec. 1971.

[10]Er-El, J., and Seginer, A., "Vortex Trajectories and Breakdown on Wing-Canard Configurations," *Journal of Aircraft*, Vol. 22, No. 8, 1985, pp. 641–648.

[11]Calarese, W., "Vortex Interaction on a Canard-Wing Configuration," Air Force Wright Aeronautical Lab., AFWAL-TR-86-3100, Wright-Patterson AFB, OH, Oct. 1986.

[12]Allen, J. M., Hernandez, G., and Lamb, M., "Body Surface Pressure Data on Two Monoplane-Wing Missile Configurations with Elliptical Cross Sections at Mach 2.5," NASA TM-85645, Sept. 1983.

[13]Priolo, F. J., and Wardlaw, J. R., "Supersonic Tactical Missile Computations Using Euler's Equations with Crossflow Separation Modeling," *AGARD 66th Panel Symposium on Missile Aerodynamics*, 1990, pp. 6.1–6.11.

[14]Ying, S. X., Steger, J. L., Schiff, L. B., and Baganoff, D., "Numerical Simulation of Unsteady, Viscous High-Angle-of-Attack Flows Using a Partially Flux-Split Algorithm," AIAA Paper 86-2179, June 1986.

[15]Steger, J. L., and Warming, R. F., "Flux Vector Splitting of the Inviscid Gas Dynamic Equations with Applications to Finite-Difference Methods," *Journal of Computational Physics*, Vol. 40, April 1981, pp. 263–293.

[16]Baldwin, B. S., and Lomax, H., "Thin Layer Approximation and Algebraic Model for Separated Turbulent Flows," AIAA Paper 78-275, Jan. 1978.

[17]Degani, D., and Schiff, L. B., "Computation of Turbulent Supersonic Flows around Pointed Bodies Having Crossflow Separation," *Journal of Computational Physics*, Vol. 66, No. 1, 1986, pp. 173–196.

[18]Ekaterinaris, J. A., and Schiff, L. B., "Numerical Predictions of Vortical Flows over Slender Delta Wings," *Journal of Aircraft*, Vol. 30, No. 6, 1993, pp. 935–942.

[19]Ekaterinaris, J. A., and Schiff, L. B., "Numerical Investigation of the Effects of Variation of Angle of Attack and Sweep Angle on Vortex Breakdown over Delta Wings," AIAA Paper 90-3000, Aug. 1990.

J. M. Allen
Associate Editor